Supplementary Information

Visualizing Nexus of Porous Architecture and Reactive Transport in Heterogeneous Catalysis by Deep Learning Computer Vision and Transfer Learning

Yuan Yu [a], Baoli Wu [b], Rui Wei [a] , Nanqi Ren [a], Shijie You [a,*]

[a] *State Key Laboratory of Urban-rural Water Resource and Environment, School of Environment, Harbin Institute of Technology, Harbin 150090, China*

[b] *North China Municipal Engineering Design and Research Institute Corporation Limited, Tianjin 300381, China*

Corresponding author:

* Shijie You

Address: P. O. Box 2603#, No. 73, Huanghe Road, Nangang District, Harbin, 150090, China.

Tel.: +86-451-86282008; Fax: +86-451-86282110

E-mail: sjyou@hit.edu.cn

Summary

Number of Pages: Page S1–Page 30

Number of Pages for Texts: Page S3–Page S6

Number of Figures: 20, Supplementary Figure 1– Supplementary Figure 20

Number of Tables: 2, Supplementary Table 1– Supplementary Table 2

Number of Pages for References: Page S30–Page S30

1. Texts

Text S1 Algorithmic logic for Quartet Structure Generation Set (QSGS) method

For geometric models of porous media, it is generated using the quartet structure generation set (QSGS) method, a popular method in the porous media field[1,2]. Detailed descriptions of this method can be found in the literature, and we only outline its key steps:

1) The computational domain is partitioned into square cells;

2) Solid "seeds" are randomly distributed in the domain based on a distribution probability, *cd*, which is smaller than the target porosity of the porous media. This is accomplished by assigning a random number to each cell and the cells whose assigned random number are less than *cd* are selected as the "seeds".

3) Grow the "seeds" to their neighboring cells based on the directional growth probability, *Pi*. To this end, a random number is assigned to each of the neighboring cell of a solid seed. If the random number of a neighboring cell is less than *Pi*, it will become part of the growing solids.

4) Repeat steps (2) and (3) until the target porosity is reached in the domain.

Together, the above steps produce binary matrix of porous media. For example, the cross section in created random structure can be described by a binary image in Supplementary Fig. 14 in which each pixel is either a pore or solid node and is denoted with a binary value of 0 (pore space) or 1 (solid phase).

Text S2 Initial/boundary conditions for numerical model

The initial values of pressure and flow velocity were set as 0 Pa and 0 m s^{-1}, respectively. The initial concentration was c_0. Moreover, the boundary conditions can be classified as inflow boundary, outflow boundary, periodic boundaries, and reactive and zero-flux boundaries. To clarify the boundary conditions and their directions, we first defined the coordinate axes based on the anisotropic growth directions:

The origin is set at the midpoint of the cube, with the positive x-axis aligned with growth direction 1, the positive y-axis with direction 2, and the positive z-axis with direction 3. The axis dimensions correspond to the number of pixels. This setup results in six possible flow directions perpendicular to the cube's faces: x+ (along direction 1), x- (along direction 3), y+ (along direction 2), y- (along direction 4), z+ (along direction 5), and z- (along direction 6).

Taking flow in the x+ direction as an example, the boundary conditions (Supplementary Fig. 19) are set as follows:

The inflow boundary is located on the yz-plane at x = -128 pixels, with flow in the positive x direction at a velocity.

$$\mathbf{u} = -V_{in} \cdot \mathbf{n} \quad \text{(Dirichlet boundary condition)} \tag{S1a}$$

$$c = c_0 \quad \text{(Dirichlet boundary condition)} \tag{S1b}$$

Where V_{in} corresponded to inlet velocity calculated by Reμ/L, in which Re = 0.1, 1, or 10; μ was (Pa s) kinematic viscosity; L was characteristic length calculated by π/s_A, and s_A was the specific surface area.

The outflow boundary is located on the yz-plane at x = 128 pixels, with zero pressure and zero concentration, allowing free outflow based on the computed pressure and concentration gradients.

$$p = 0 \quad \text{(Dirichlet boundary condition)} \tag{S2a}$$

$$\mathbf{n} \cdot \left(-D\nabla c\right) = 0 \quad \text{(Dirichlet boundary condition)} \tag{S2b}$$

Two pairs of periodic boundaries were set perpendicular to the flow direction. The first pair is on the xz-planes at y = 128 and y = -128 pixels, and the second pair is on the xy-planes at z = 128 and z = -128 pixels. This setup assumes that fluid or substances exiting one boundary re-enter through the opposite boundary in the same state, which simulates continuous flow within the porous structure and reflects the infinite expansibility of the porous medium.

$$\mathbf{u}\left(y = 0, x, z\right) = \mathbf{u}\left(y = 128\,pixel, x, z\right) \quad \text{(periodic boundary condition)} \tag{S3a}$$

$$\mathbf{c}\left(y = 0, x, z\right) = \mathbf{c}\left(y = 128\,pixel, x, z\right) \quad \text{(periodic boundary condition)} \tag{S3b}$$

$$\mathbf{u}\left(z = 0, x, y\right) = \mathbf{u}\left(z = 128\,pixel, x, y\right) \quad \text{(periodic boundary condition)} \tag{S3c}$$

$$\mathbf{c}\left(z = 0, x, y\right) = \mathbf{c}\left(z = 128\,pixel, x, y\right) \quad \text{(periodic boundary condition)} \tag{S3d}$$

The remaining boundaries are set as reactive and zero-flux boundaries. According to equation S4a-b, this means that no fluid or substances flow out at these boundaries, and the substances are consumed at a rate calculated by the equation.

$$\mathbf{u} = 0 \quad \text{(Dirichlet boundary condition)} \tag{S4a}$$

$$-\mathbf{n} \cdot \left(-D\nabla c\right) = -D\frac{Da}{L}c \quad \text{(Neumann boundary condition)} \tag{S4b}$$

Where D ($m^2\ s^{-1}$) corresponded to diffusion coefficient; c was concentration.

Text S3 The impact of connectivity on model performance

As shown in Fig. 3h and Supplementary Fig. 20, some disconnected pores remained connected across slices. The concentration prediction from cGAN-FRT captured this inter-slice connectivity (Supplementary Fig. 20), demonstrating its ability to detect pore connectivity. This capability stemmed from the cGAN using all slices as input, enabling it to learn the spatial relationships between the pores.

2. Figures

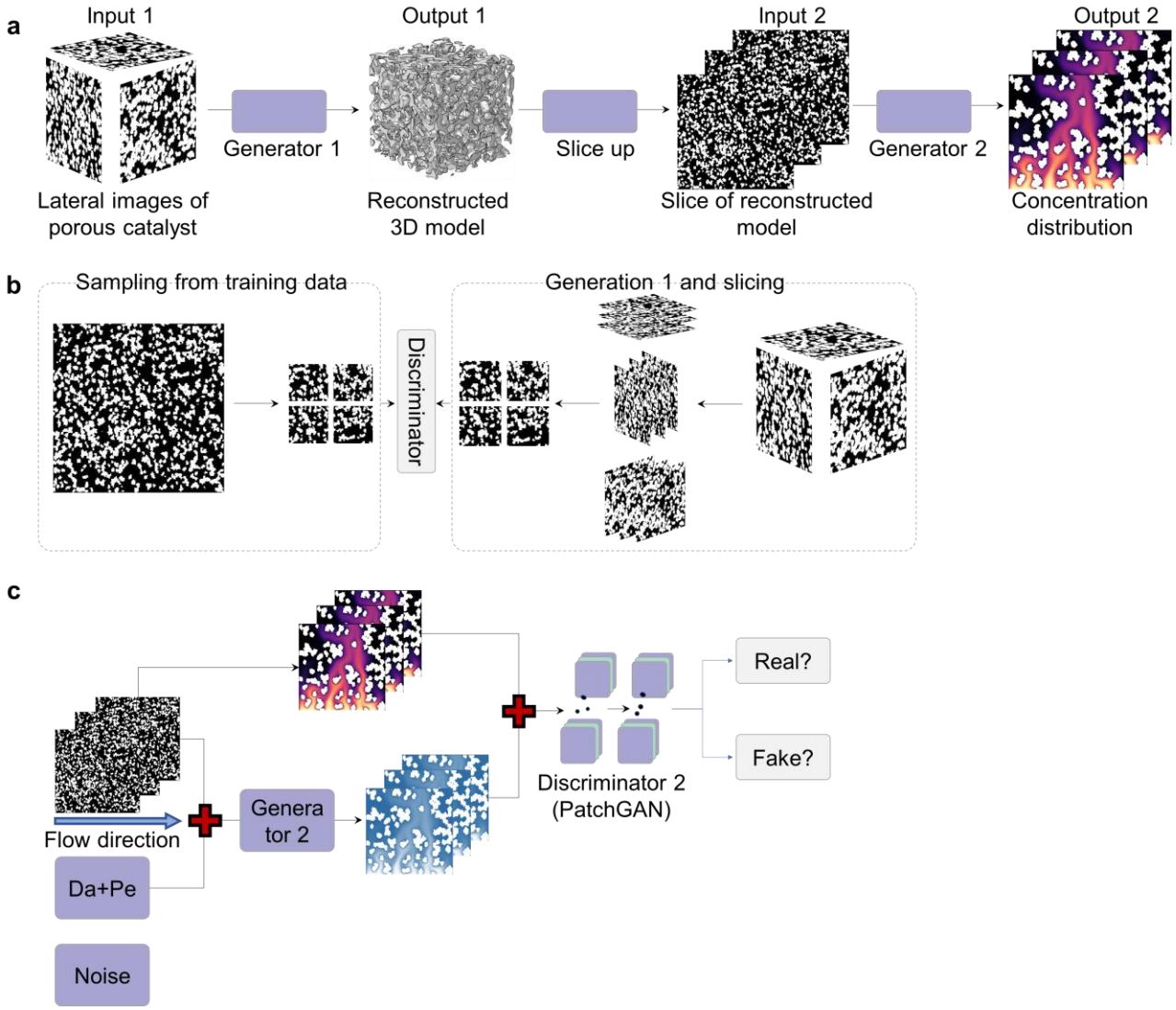

Supplementary Fig. 1 | Model architecture for cGAN-FRT. **a**, two-steps workflow. **b**, Architecture for Generator 1. **c**, Architecture for Generator 2.

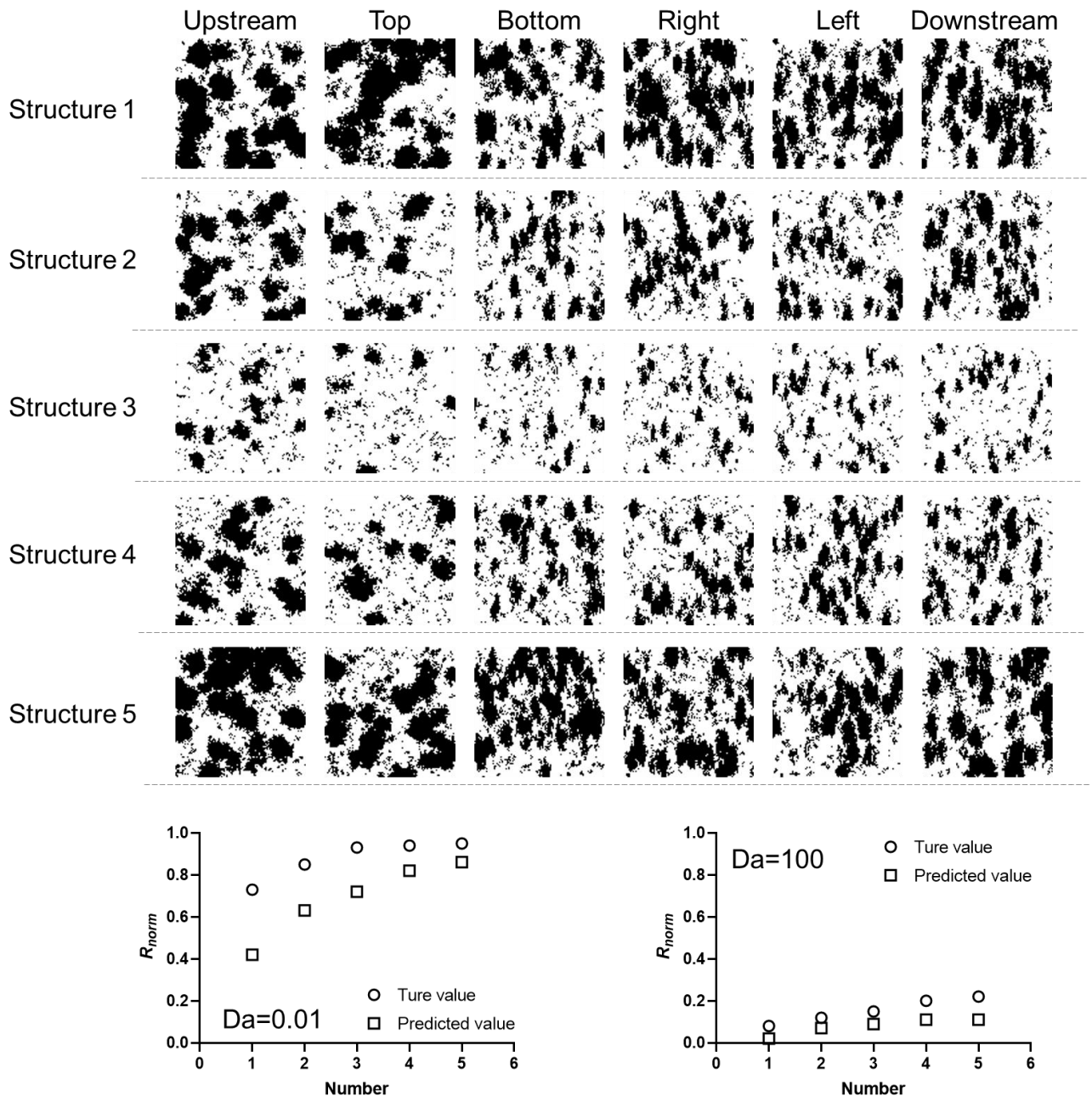

130

131 **Supplementary Fig. 2 |** Five anisotropic porous architectures with g_i (i=1-4) set to 0.005 and the

132 accuracy for direct prediction of normalized effective reaction rate (R_{norm}) with source model.

133

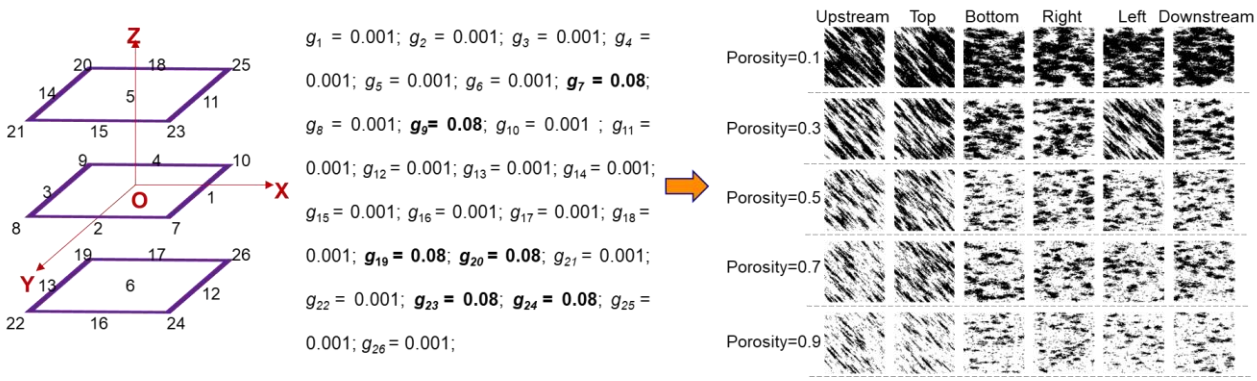

Supplementary Fig. 3 | Anisotropy factor value (g_i) and example of images in transfer dataset used in Fig. 3b and c.

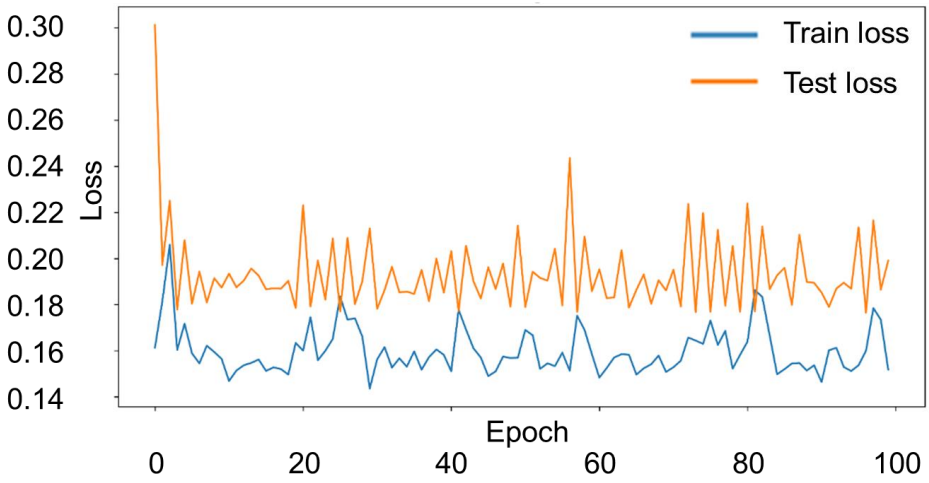

Supplementary Fig. 4 | Training performance on a small-scale dataset from scratch without transfer learning.

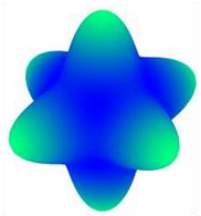

g_1 = 0.08; g_2 = 0.08; g_3 = 0.08; g_4 = 0.08;

g_5 = 0.08; g_6 = 0.08; g_7 = 0.001; g_8 = 0.001;

g_9= 0.001; g_{10} = 0.001 ; g_{11} = 0.001; g_{12} = 0.001; g_{13} = 0.001;

g_{14} = 0.001; g_{15} = 0.001; g_{16} = 0.001; g_{17} = 0.001; g_{18} = 0.001;

g_{19} = 0.001; g_{20} = 0.001; g_{21} = 0.001; g_{22} = 0.001; g_{23} = 0.001;

g_{24} = 0.001; g_{25} = 0.001; g_{26} = 0.001;

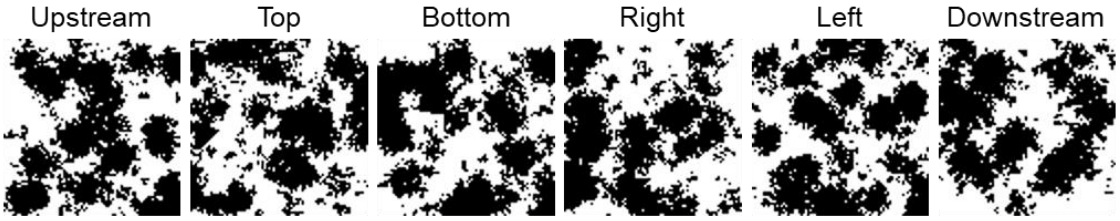

Porosity:0.3; Tortuosity in x direction: 1.25; Coordination number: 4.5; Throat radius: 4.1; Throat length: 17.3; Specific surface: 1.2×10^{-4}; Grain sphericity: 0.77; Grain radius: 8.73;

143

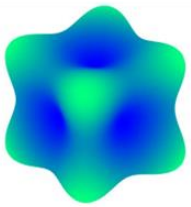

g_1 = 0.001; g_2 = 0.001; g_3 = 0.001; g_4 = 0.001;

g_5 = 0.001; g_6 = 0.001; g_7 = 0.001; g_8 = 0.001; g_9= 0.001; g_{10} = 0.001 ; g_{11} = 0.001; g_{12} = 0.001; g_{13} = 0.001; g_{14} = 0.001; g_{15} = 0.001; g_{16} = 0.001; g_{17} = 0.001; g_{18} = 0.001; **g_{19} = 0.08; g_{20} = 0.08; g_{21} = 0.08; g_{22} = 0.08; g_{23} = 0.08; g_{24} = 0.08; g_{25} = 0.08; g_{26} = 0.08;**

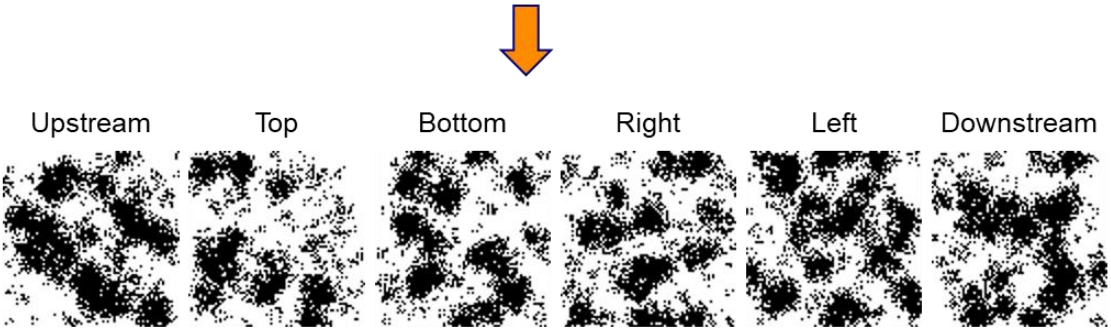

Porosity:0.3; Tortuosity in x direction: 1.21; Coordination number: 4.5; Throat radius: 3.8; Throat length: 17.2; Specific surface: 1.3×10^{-4}; Grain sphericity: 0.71; Grain radius: 7.81;

144

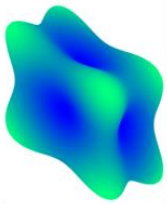

g_1 = 0.001; g_2 = 0.001; g_3 = 0.001; g_4 = 0.001;

g_5 = 0.001; g_6 = 0.001; g_7 = 0.001; **g_8 = 0.08**; g_9= 0.001; **g_{10} = 0.08** ;

g_{11} = 0.001; g_{12} = 0.001; g_{13} = 0.001; g_{14} = 0.001; g_{15} = 0.001; g_{16} = 0.001; g_{17} = 0.001; g_{18} = 0.001; g_{19} = 0.001; g_{20} = 0.001; **g_{21} = 0.08**; **g_{22} = 0.08**; g_{23} = 0.001; g_{24} = 0.001; **g_{25} = 0.08**; **g_{26} = 0.08**;

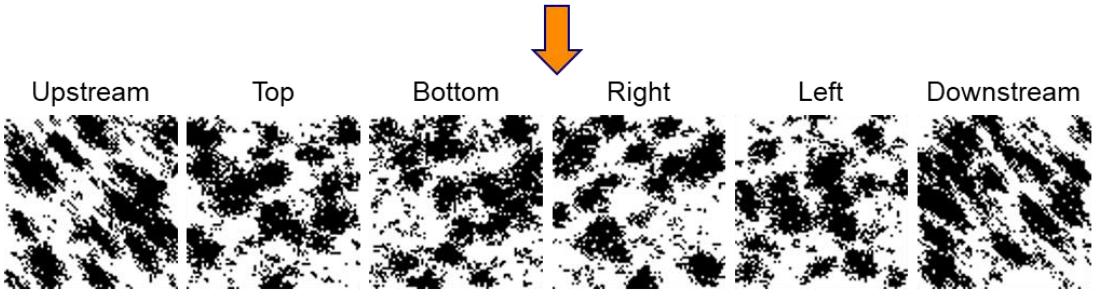

Porosity:0.3; **Tortuosity in x direction**: 1.60; Coordination number: 5.7; Throat radius: 3.5; Throat length: 15.9; Specific surface: 1.4×10^{-4}; Grain sphericity: 0.36; Grain radius: 6.63;

Porosity:0.3; **Tortuosity in y direction**: 1.32; Coordination number: 5.7; Throat radius: 3.5; Throat length: 15.9; Specific surface: 1.4×10^{-4}; Grain sphericity: 0.36; Grain radius: 6.63;

145

146 **Supplementary Fig. 5 |** Anisotropy factor value (g_i), images and quantitative structural features

147 (QSFs) for three kinds of structures used in Figure 4.

148

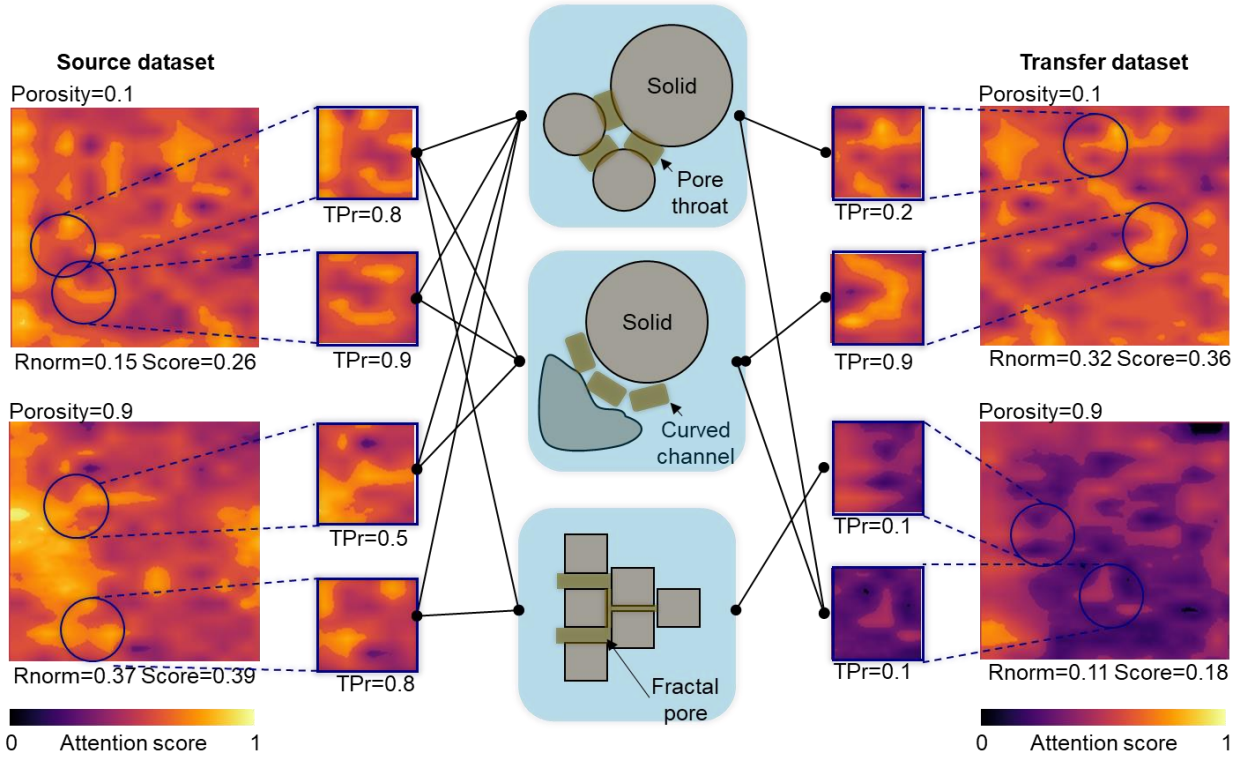

149

150 **Supplementary Fig. 6 |** Heat maps for source and transfer conditions with 0.1 porosity and different

151 throat-to-pore ratio (TPr).

152

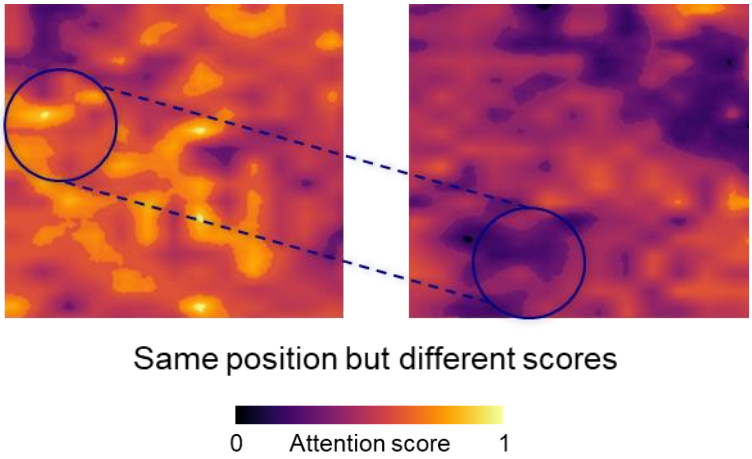

153

154

155 **Supplementary Fig. 7 |** Attention variations when changing fluid direction.

156

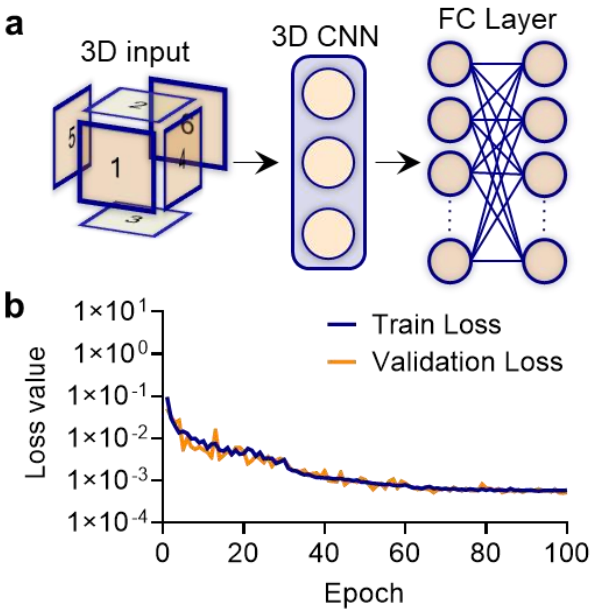

Supplementary Fig. 8 | Pre-training performance on the source dataset. a, Framework and **b,** Learning curves for Three-Dimensional Convolutional Neural Network (3DCNN).

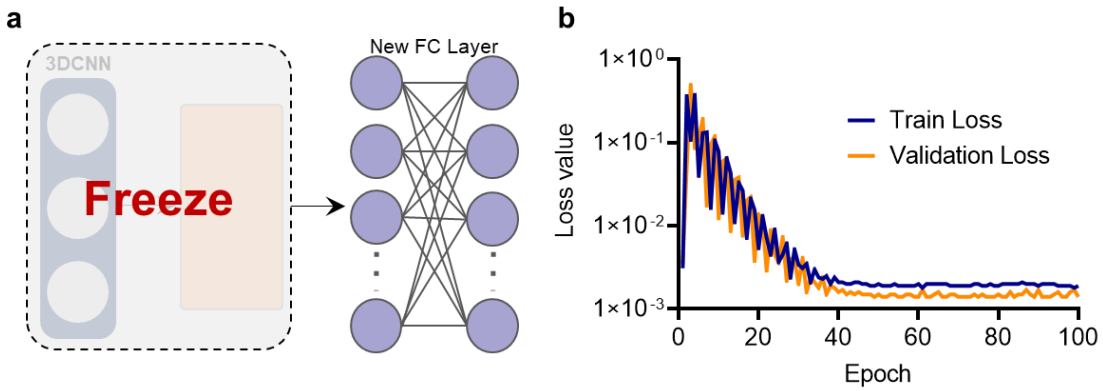

Supplementary Fig. 9 | Transfer Learning Performance. a, Schematic representation of FRT strategy for Three-Dimensional Convolutional Neural Network (3DCNN). **b,** Learning curves.

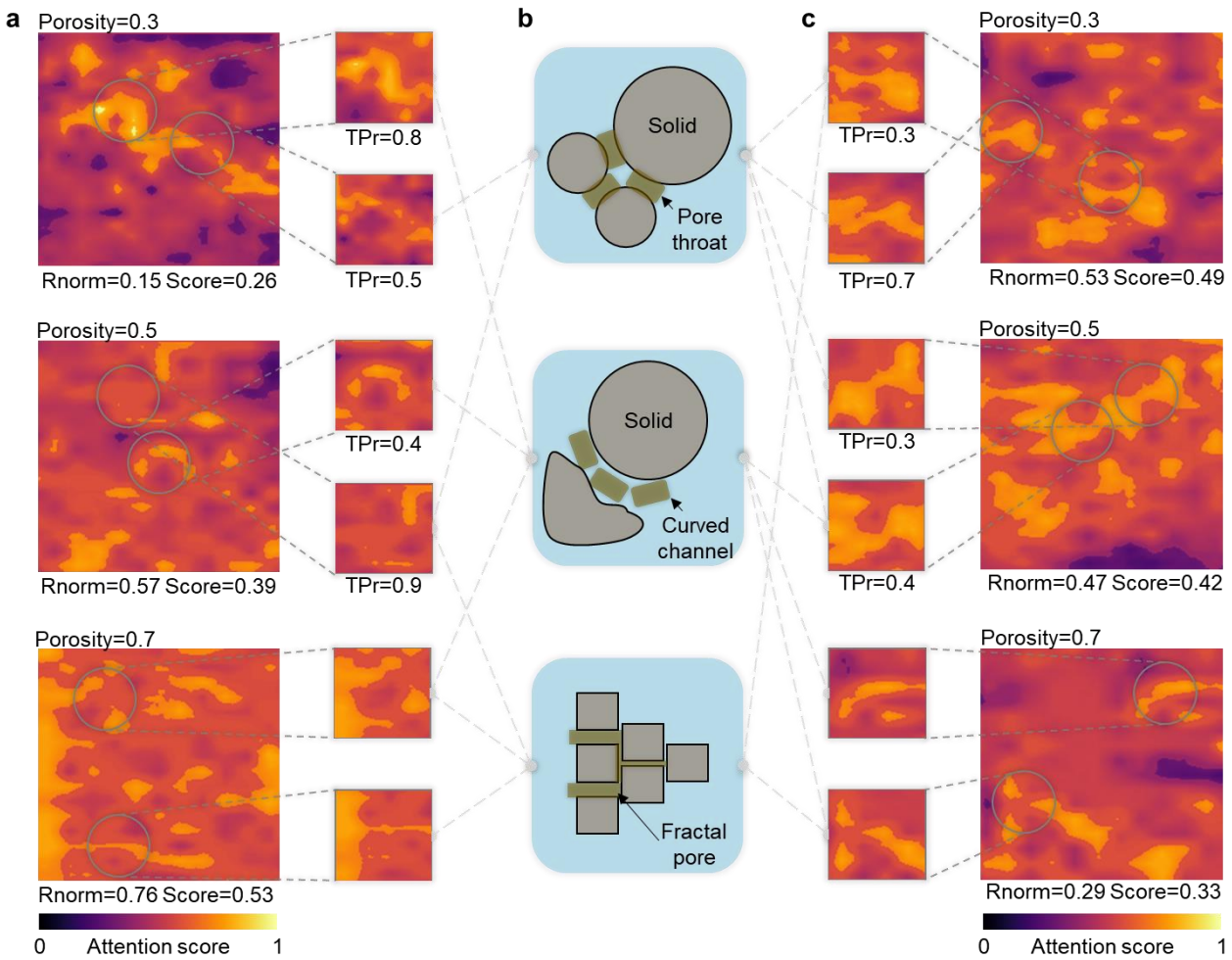

Supplementary Fig. 10 | Variation of R_{norm} by attention analysis of Three-Dimensional Convolutional Neural Network (3DCNN). **a,** Heat maps for isotropic architectures with different porosities. **b,** Structural features for high-attention regions. **c,** Heat maps for anisotropic architectures with different porosities.

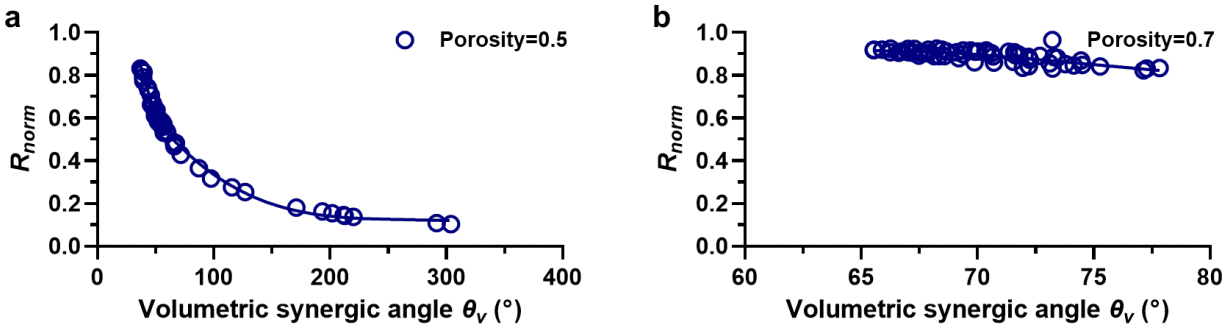

174

175 **Supplementary Fig. 11 |** Relationship between average synergic angle (θ_V) and normalized effective

176 reaction rate (R_{norm}) for different conditions: **a,** Porosity= 0.5, **b,** Porosity= 0.7.

177

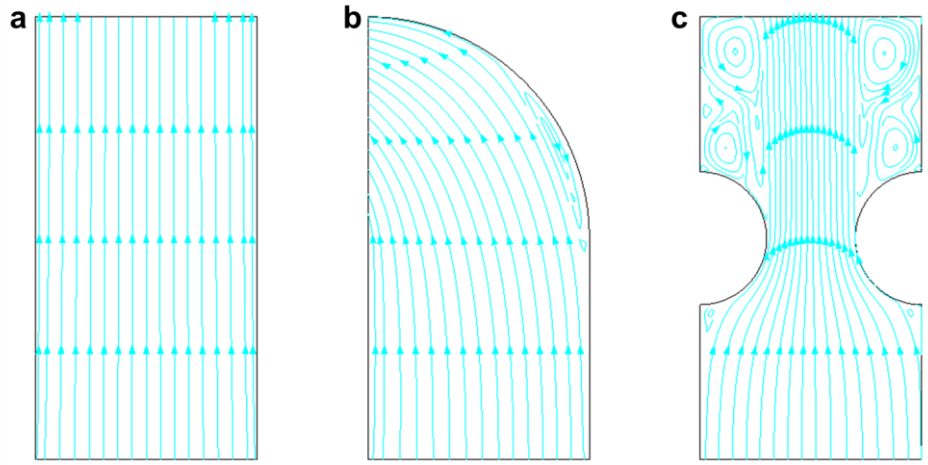

178

179 **Supplementary Fig. 12 | Streamline distribution inside these various channels. a,** Flat channels

180 (θ >= 90), **b,** Curved channels (60 <θ< 90); **c,** Pore throat (θ< 60).

181

182

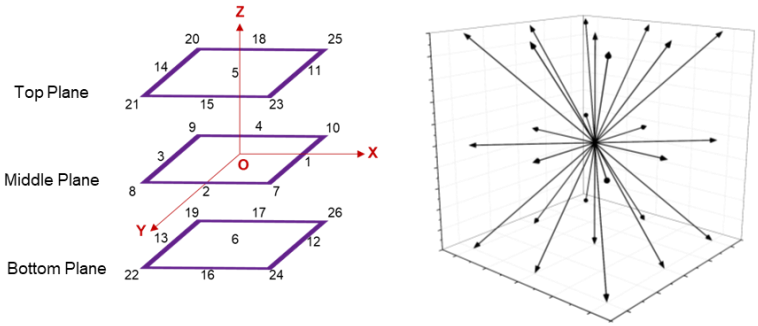

Supplementary Fig. 13 | Diagram of the 26 growth directions: from the center of the cube to each edge midpoint, vertex, and face center. x+ (direction 1), x- (direction 3), y+ (direction 2), y- (direction 4), z+ (direction 5), and z- (direction 6). Azimuthal angle and elevation angle for each direction were given in Table S1.

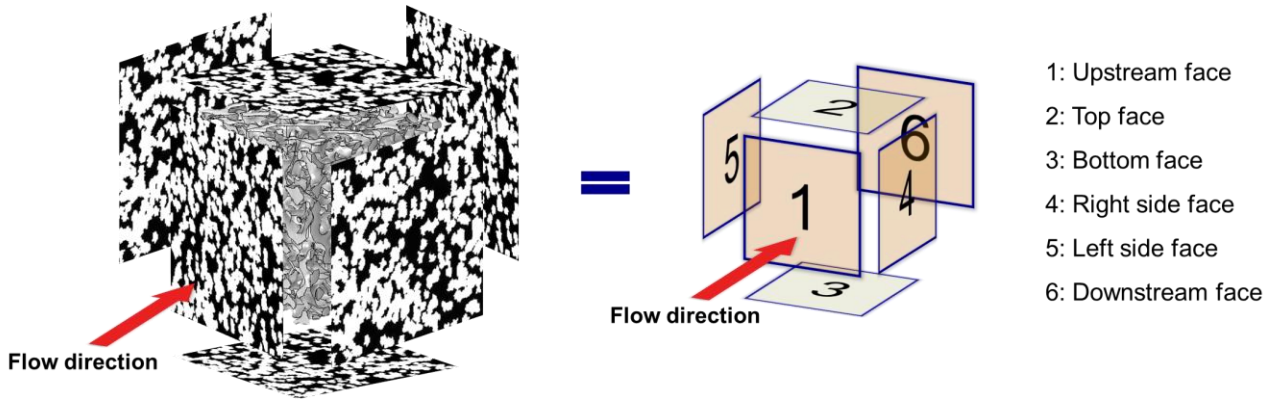

Supplementary Fig. 14 | The six typical lateral images from created random structure based on QSGS algorithm, where white and black regions represent solid and pore phases, respectively.

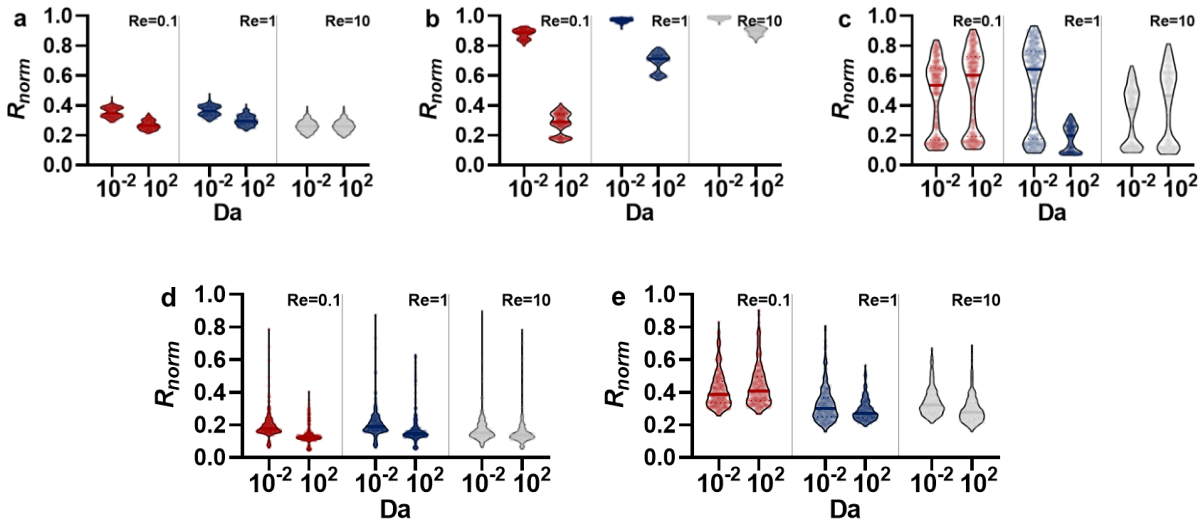

Supplementary Fig. 15 | Data structure analysis for source dataset. **a,** Porosity= 0.1; **b,** Porosity= 0.3; **c,** Porosity= 0.5; **d,** Porosity= 0.7 and **e,** Porosity= 0.9.

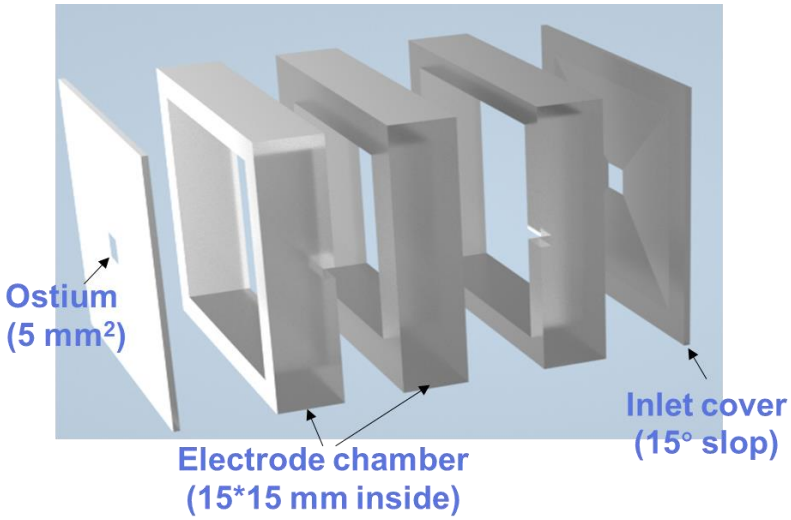

Supplementary Fig. 16 | Detailed dimensions and structure for reactor.

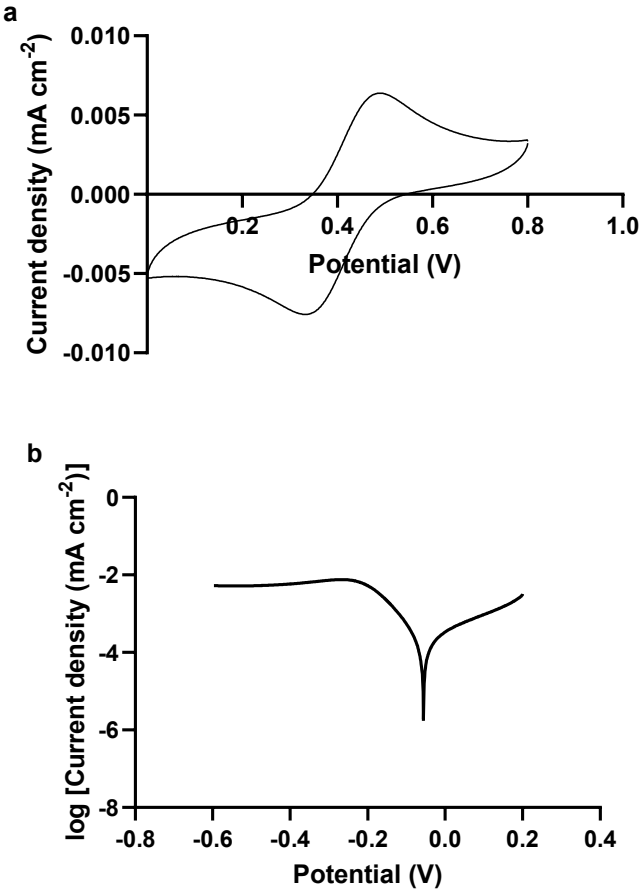

Supplementary Fig. 17 | a, Cyclic voltammetry curve and, **b,** Tafel plots for the electrocatalysis system.

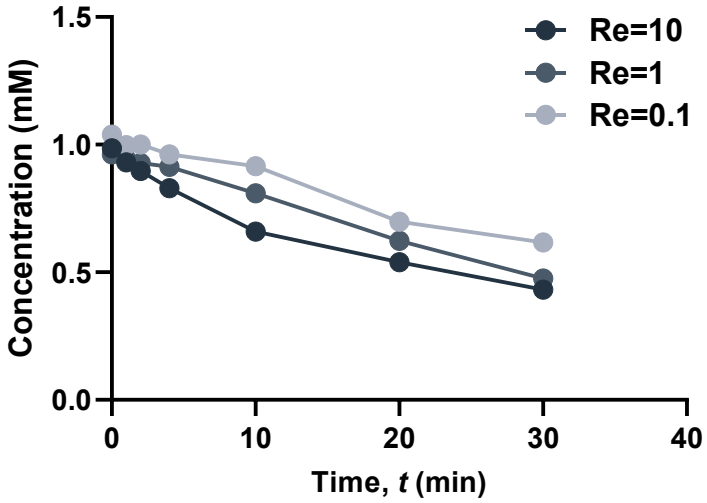

211

212 **Supplementary Fig. 18 |** Concentration-time curve measured in electrocatalytic reduction of

213 potassium ferricyanide using foam nickel electrodes.

214

215

216

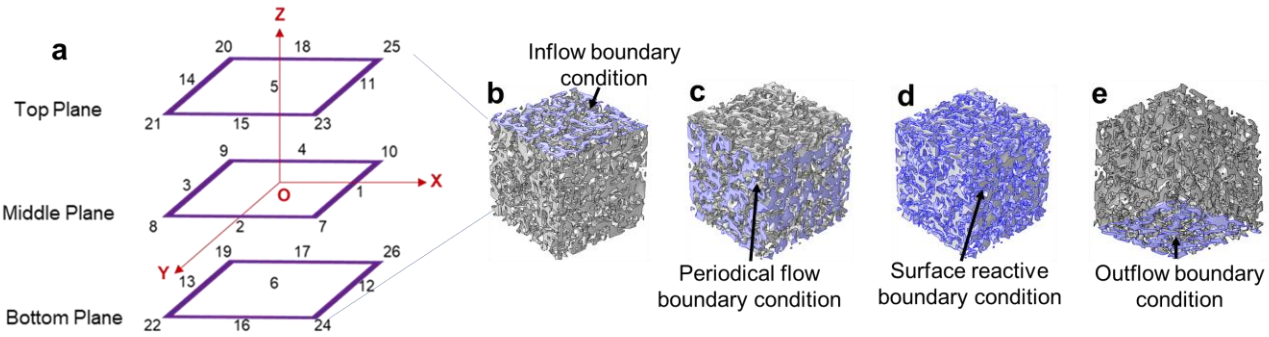

Supplementary Fig. 19 | Location of boundary condition: **a,** Coordinate axes based on the anisotropic growth directions; **b,** Inflow boundary condition; **c,** Periodical boundary condition; **d,** Reactive and zero flux boundary condition; **e,** Outflow boundary condition.

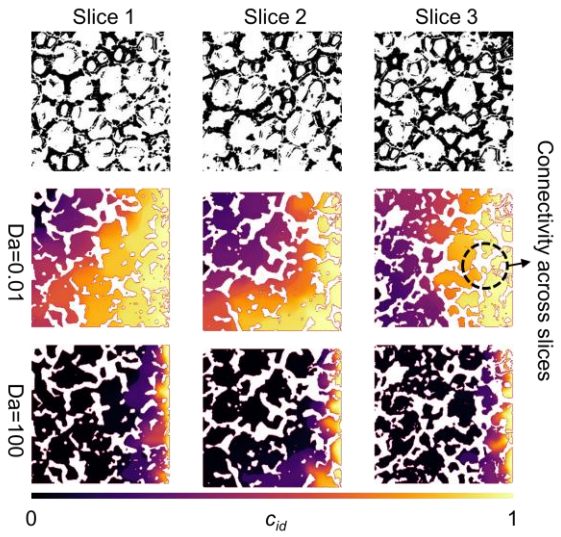

Supplementary Fig. 20 | Porous structure and cGAN-FRT concentration predictions showing inter-slice connectivity. Normalized concentration field (c_{id}) was calculated by $c_{id}=c_i/c_0$, where c_i and c_0 represented the local and initial concentration, respectively.

3. Tables

Table S1 Azimuthal angle and elevation angle for 26 directions in Fig. S2.

Direction Number	Direction (x, y, z)	Aziumth (°)	Elevation (°)
1	(1, 0, 0)	0	90
2	(0, 1, 0)	90	90
3	(-1, 0, 0)	180	90
4	(0,-1, 0)	-90	90
5	(0, 0, 1)	0	0
6	(0, 0, -1)	0	180
7	(1, 1, 0)	45	90
8	(-1, 1, 0)	135	90
9	(-1, -1, 0)	-135	90
10	(1, -1, 0)	-45	90
11	(1, 0, 1)	0	45
12	(1, 0, -1)	0	135
13	(-1, 0, -1)	180	135
14	(-1, 0, 1)	180	45
15	(0, 1, 1)	90	45
16	(0, 1, -1)	90	135
17	(0, -1, -1)	-90	135
18	(0, -1, 1)	-90	45
19	(-1, -1, -1)	-135	125.3
20	(-1, -1, 1)	-135	54.8
21	(-1, 1, 1)	135	54.7

22	(-1, 1, -1)	135	125.3
23	(1, 1, 1)	45	54.7
24	(1, 1, -1)	45	125.3
25	(1, -1, 1)	-45	54.7
26	(1, -1, -1)	-45	125.3

*Azimuthal angle (θ_{AA}) is the angle between the projection of the vector onto the *xy*-plane and the positive *x*-axis, defined as θ_{AA}=arctan(*y*/*x*);
*Elevation angle (θ_{EA}) is the angle between the vector and the positive *z*-axis, defined as θ_{AA}=arccos(*z*/*r*). Where *r* is the magnitude of the vector.

Table S2 Physical parameters of materials used in simulation.

Parameter	Value
Density, ρ (kg m^{-3})	997.6 [$K_4Fe(CN)_6$]; 1000 [KCl]
kinematic viscosity, μ (Pa s)	0.889×10^{-3} [$K_4Fe(CN)_6$]; 0.89×10^{-3} [KCl]
Diffusion coefficient, D (m^2 s^{-1})	7.2×10^{-10} [$K_4Fe(CN)_6$]; 1.0×10^{-9} [KCl]
Initial concentration, c_0 (mol L^{-1})	1.5×10^{-3} [$K_4Fe(CN)_6$]; 1×10^{-3} [KCl]

References

1. Lu, G., Lu, G.Q. & Xiao, Z.M. Mechanical Properties of Porous Materials. *Journal of Porous Materials* **6**, 359-368 (1999).
2. Guan, D., Wu, J.H. & Jing, L. A statistical method for predicting sound absorbing property of porous metal materials by using quartet structure generation set. *Journal of Alloys and Compounds* **626**, 29-34 (2015).